



Article

# Low-Frequency Noise Characteristics of Graphene/h-BN/Si Junctions

Justinas Glemža <sup>1</sup>, Ingrida Pliaterytė <sup>1</sup>, Jonas Matukas <sup>1</sup>, Rimantas Gudaitis <sup>2</sup>, Andrius Vasiliauskas <sup>2</sup>, Šarūnas Jankauskas <sup>2</sup> and Šarūnas Meškinis <sup>2</sup>,\*

- Institute of Applied Electrodynamics and Telecommunications, Vilnius University, Saulėtekio 3, LT-10257 Vilnius, Lithuania; justinas.glemza@ff.vu.lt (J.G.); ingrida.pliateryte@ff.stud.vu.lt (I.P.); jonas.matukas@ff.vu.lt (J.M.)
- Institute of Materials Science, Kaunas University of Technology, K. Baršausko 59, LT-51423 Kaunas, Lithuania; rimantas.gudaitis@ktu.lt (R.G.); andrius.vasiliauskas@ktu.edu (A.V.); sarunas.jankauskas@ktu.lt (Š.J.)
- \* Correspondence: sarunas.meskinis@ktu.lt

#### **Abstract**

Graphene/h-BN/Si heterostructures show considerable potential for future use in infrared detection and photovoltaic technologies due to their adjustable electrical behavior and well-matched interfacial structure. The near-lattice match between graphene and hexagonal boron nitride (h-BN) enables the deposition of low-defect-density graphene on h-BN surfaces. This study presents a thorough exploration of the low-frequency electrical noise behavior of graphene/h-BN/Si heterojunctions under both forward and reverse bias conditions at room temperature. Graphene nanolayers were directly grown on h-BN films using microwave plasma-enhanced CVD. The h-BN layers were formed by reactive highpower impulse magnetron sputtering (HIPIMS). Four h-BN thicknesses were examined: 1 nm, 3 nm, 5 nm, and 15 nm. A reference graphene/Si junction (without h-BN) prepared under identical synthesis conditions was also studied for comparison. Low-frequency noise analysis enabled the identification of dominant charge transport mechanisms in the different device structures. Our results demonstrate that grain boundaries act as dominant defects contributing to increased noise intensity under high forward bias. Statistical analysis of voltage noise spectral density across multiple samples, supported by Raman spectroscopy, reveals that hydrogen-related defects significantly contribute to 1/f noise in the linear region of the junction's current-voltage characteristics. This study provides the first in-depth insight into the impact of h-BN interlayers on low-frequency noise in graphene/Si heterojunctions.

**Keywords:** defects; fluctuations; directly synthesized graphene/h-BN/Si junction; hexagonal boron nitride; microwave PECVD; high power impulse magnetron sputtering; low-frequency noise; Raman spectroscopy

# check for updates

Academic Editor: Heinz Christoph Neitzert

Received: 20 July 2025 Revised: 17 August 2025 Accepted: 20 August 2025 Published: 22 August 2025

Citation: Glemža, J.; Pliaterytė, I.; Matukas, J.; Gudaitis, R.; Vasiliauskas, A.; Jankauskas, Š.; Meškinis, Š. Low-Frequency Noise Characteristics of Graphene/h-BN/Si Junctions. Crystals 2025, 15, 747. https:// doi.org/10.3390/cryst15090747

Copyright: © 2025 by the authors. Licensee MDPI, Basel, Switzerland. This article is an open access article distributed under the terms and conditions of the Creative Commons Attribution (CC BY) license (https://creativecommons.org/licenses/by/4.0/).

# 1. Introduction

Nearly two decades after its initial isolation from graphite, graphene remains among the most intensively investigated materials across contemporary physical sciences, nanotechnology, and materials research. It has attracted significant attention as a key material for future electronic and photonic technologies owing to a unique combination of high optical transparency and electrical conductivity, superior charge carrier mobility, and outstanding thermal conductivity [1–4].

Crystals **2025**, 15, 747 2 of 16

Importantly, heterostructures combining graphene with conventional semiconductors of IV and III–V groups have been realized [3,5–10]. Benefiting from the mature and scalable silicon semiconductor technology, graphene/Si heterojunctions exhibit promising potential for solar cells, broadband photodetectors, and gas sensing applications [1,11–17].

A notable advantage of these junctions is their ability to enhance silicon solar cells' sub-bandgap infrared conversion efficiency [18] and extend the operating band of Si-based photonics into the mid-infrared spectral range [16,19,20]. Despite the potential, graphene/Si junctions still face unresolved issues such as variability in ideality factors, Schottky barrier height inhomogeneity, and limited performance due to various interface defects, such as dangling bonds at the silicon surface [11,12,14,17,21].

Due to its sensitivity to structural imperfections and defects introduced during sample fabrication or device operation, low-frequency noise spectroscopy serves as a non-invasive and powerful diagnostic approach for characterizing electronic and optoelectronic devices [22–24]. Different types of noise can be categorized, including thermal (also known as Johnson or Nyquist) noise, which is caused by the random motion of charge carriers and has a "white" spectrum, i.e., is frequency independent. Shot noise is also characterized by a "white" spectrum and results from uncorrelated and stochastic transitions of charge carriers through a potential energy barrier.

Generation-recombination noise, which is distinguished by a Lorentzian-type spectrum, and flicker or 1/f noise arise from fluctuations in the conductance [23,25,26]. Among these, 1/f noise is particularly important for assessing device reliability and gaining insight into carrier transport mechanisms [22,23,26].

In practical applications, low-frequency fluctuations can fundamentally limit sensor sensitivity. The 1/f noise in graphene is generally attributed to correlated variations in the number of charge carriers and their mobility [26–30]. Flicker noise in graphene-based semiconductor devices is under intensive investigation because of its impact on real-world device performance [3,6,27,28,30–34]. However, only limited studies have specifically investigated low-frequency noise characteristics in graphene/silicon junctions [3,6,35]. These works validate the significance of 1/f noise, which is sometimes omitted and only shot noise is considered, in estimating photodetector parameters such as noise equivalent power. Together with Raman spectroscopy, low-frequency noise investigation is a powerful tool not only for defect density evaluation [35] but also for defect identification as this study aims to demonstrate.

The defect density in graphene is highly sensitive to the synthesis method [36]. Graphene can be directly deposited on Si substrates without the use of catalysts, employing plasma-enhanced chemical vapor deposition (PECVD). The key benefit of this approach is avoiding lengthy transfer procedures as well as associated contamination and mechanical damage [37]. However, such directly grown graphene is usually nanocrystalline and contains a high density of grain-boundary defects [38,39]. These defects can significantly limit the performance and reliability of devices and sensors based on directly synthesized graphene [40]. While grain boundaries as noise sources have been investigated earlier in graphene transistors [30], this study also reveals their impact on the rapid noise increase in graphene/Si structures with an inserted hexagonal boron nitride interlayer. Careful substrate selection can substantially reduce the density of grain boundaries and other defects, thereby improving material quality.

The near-lattice match between graphene and hexagonal boron nitride (h-BN) enables epitaxial growth of low-defect-density graphene [41–44]. It is noteworthy that graphene/silicon solar cell conversion efficiency may be raised more than three times by inserting an h-BN interlayer [1,13]. However, to date, graphene epitaxy on h-BN has primarily been employed using exfoliated hexagonal boron nitride flakes or h-BN films

Crystals **2025**, 15, 747 3 of 16

synthesized by CVD on Cu foils. Several recent studies described graphene synthesis on h-BN films directly deposited on substrates commonly used for semiconductor device fabrication, such as silicon or SiO<sub>2</sub>; however, lower defect density in graphene was not achieved [4,45]. Despite this, significant improvements in the graphene/h-BN/silicon devices' photoelectric and photovoltaic properties were found compared to the graphene/Si junction [4].

Notably, a graphene-channel field-effect transistor (FET) fabricated on a boron nitride substrate and encapsulated by another boron nitride layer exhibited ultralow low-frequency noise [32]. Noise in such a device was much lower compared to the graphene-based FET fabricated on the commonly used SiO<sub>2</sub> substrate [33]. Nevertheless, the effects of the h-BN interlayer on the low-frequency noise properties of the graphene/monocrystalline silicon heterojunction have not been studied to date. Only Ui Yeon Won et al. [46] applied noise measurements to evaluate the detectivity of the graphene/h-BN/silicon photosensor, fabricated using transferred graphene and boron nitride flakes. However, no detailed analysis of the noise behavior was reported. In such structures, determining conductivity only from temperature-dependent current–voltage characteristics can be challenging, as the dominant conduction mechanism may vary with temperature or involve multiple competing mechanisms. Here, low-frequency noise measurements can provide valuable complementary information. Based on low-frequency noise analysis, only Schottky emission was identified at the graphene/Si junctions [3].

To address the knowledge gap, this study systematically investigates low-frequency fluctuations in graphene/h-BN/Si junctions and compares them with those in conventional graphene/Si diodes. The effects of the h-BN interlayer thickness and the structural features of graphene grown on h-BN films are analyzed. Our results demonstrate that both grain boundary and on-site defects significantly affect low-frequency noise behavior. Low-frequency noise spectroscopy was used to determine dominant conduction mechanisms at room temperature, avoiding the complexity of analyzing temperature-dependent current-voltage characteristics (this is illustrated in Supplement S3 "Identification of Schottky and Poole–Frenkel emissions via current–voltage characteristics"). This study provides the first in-depth insight into how h-BN interlayers influence low-frequency noise in graphene and Si heterostructures.

# 2. Materials and Methods

The samples were prepared on single-crystalline, double-side-polished, n-type silicon (100) wafers (Sil'tronix Silicon Technologies, Archamps, France). Their resistivity values were from 1 to  $10~\Omega$ -cm. High-power impulse magnetron sputtering (HIPIMS) was applied to deposit h-BN films onto the wafers. The boron nitride films deposition conditions can be seen in Table 1. Details of the interlayer deposition parameters are summarized in Table 1. Boron nitride films growth conditions were selected considering our previous study [47]. Detailed information on the structure and composition of the h-BN films utilized in this research is available in [47]. Notably, our previous study found that the B:N ratio for thicker h-BN films was 1:1 for 30 min to grow a film of ~50 nm thickness and 1.17 for 60 min to grow a film of ~100 nm thickness [47]. The continuous h-BN film was ultra-smooth with a roughness (Rq) of ~0.5 nm [4].

Graphene was synthesized via microwave PECVD using a Cyrannus system (Innovative Plasma Systems (Iplas) GmbH, Troisdorf, Germany). To protect the samples from excessive exposure to direct plasma, a specialized enclosure was utilized [35,48,49]. Before the graphene deposition, the substrate was cleaned by hydrogen plasma activation. The substrate pre-treatment and graphene synthesis conditions are in Table 2. It is worth men-

Crystals **2025**, 15, 747 4 of 16

tioning that our previous research indicated that the roughness of graphene grown on a continuous h-BN interlayer was below 1 nm [4].

| Target | Deposition<br>Tempera-<br>ture (°C) | Impulse<br>On-time<br>(t <sub>on</sub> ) (μs) | Impulse<br>Off-time<br>(t <sub>off</sub> ) (μs) | Average<br>Impulse<br>Current (A) | Average<br>Voltage (V) | Substrate-<br>Cathode<br>Distance<br>(cm) | Interlayer<br>Thick-<br>nesses (nm) |
|--------|-------------------------------------|---|---|-----------------------------------|------------------------|---|-------------------------------------|
| Boron  | 800                                 | 17  | 150   | 1.2                               | 930                    | 15  | 1, 3, 5, 15                         |

**Table 2.** Graphene synthesis process technological parameters.

| Technological<br>Process  | Plasma Power<br>(kW) | Temperature<br>(°C) | H <sub>2</sub> Gas Flow<br>(sccm) | CH <sub>4</sub> Gas<br>Flow (sccm) | Pressure<br>(mBar) | Time<br>(min) |
|---------------------------|----------------------|---------------------|-----------------------------------|------------------------------------|--------------------|---------------|
| Graphene<br>pre-treatment | 1                    | 700                 | 200                               | 0                                  | 10                 | 10            |
| Graphene growth           | 0.7                  | 700                 | 75                                | 25                                 | 10                 | 60            |

Diodes based on graphene, hexagonal boron nitride, and silicon were fabricated to assess their electrical and low-frequency noise properties. The cross-sectional view of the device is shown in Figure 1. For more details on diode fabrication, refer to previous work [4].

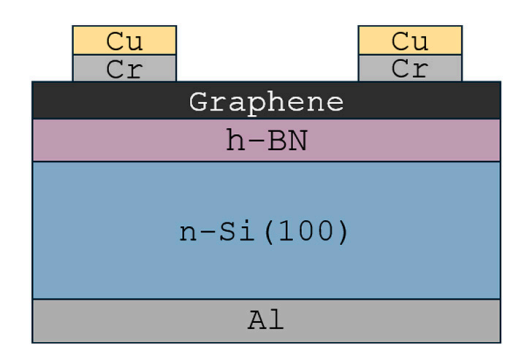


**Figure 1.** Schematic of the graphene/h-BN/Si(100) junction device.

The thickness of boron nitride films was estimated based on the deposition rate of the thicker films revealed in our previous research [47] and the corresponding growth duration.

Low-frequency noise measurements were conducted across the 10 Hz to 60 kHz frequency band under constant current conditions, for both forward and reverse bias, at ambient temperature. The noise measurement setup consists of a specially designed low-noise amplifier, filtering modules, and analog-to-digital converter PCI-6115 (National Instruments, Austin, TX, USA). The spectral density of voltage fluctuations' ( $S_U$ ) is derived by applying the Cooley–Tukey Fast Fourier Transform algorithm. All noise measurements were carried out inside a Faraday cage to minimize electromagnetic interference. A detailed noise measurement description and a schematic of the experimental setup (Figure S1) are provided in Supplement S1. Four reference graphene/Si junctions and six graphene/h-BN/Si samples were tested within each h-BN thickness category. A B1500A semiconductor parameter analyzer (Keysight, Santa Rosa, CA, USA) with minimum current measurement resolution of 100 fA was employed to acquire current–voltage (I-V) characteristics. I-V characteristics under CW operation were measured with a voltage step of 10 mV with 0 ms delay time at forward and reverse sweeps starting at 0 V. The compliance DC current was

Crystals **2025**, 15, 747 5 of 16

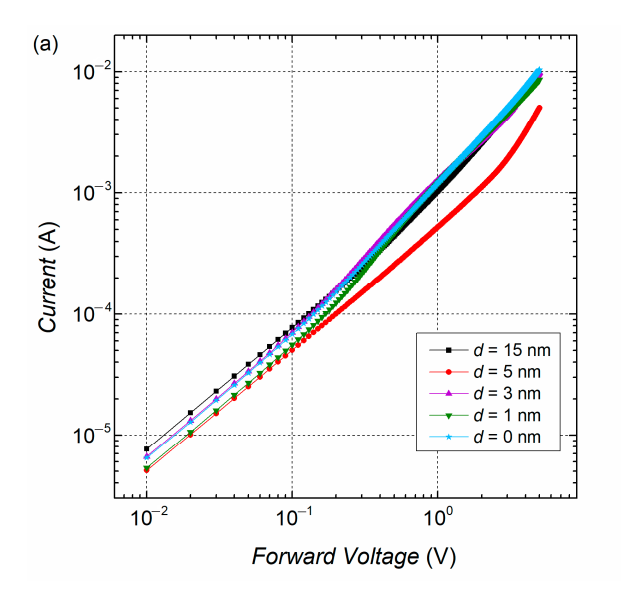
limited to 20 mA and the maximum voltage to  $\pm 5$  V to avoid the device under investigation damage. The room temperature maintained in the laboratory was 295 K.

The structural properties of the samples were analyzed with the aid of an inVia (Renishaw, United Kingdom) Raman spectrometer. The exciting laser wavelength of 532 nm was applied. We used a laser power of 1.5 mW for measurements. Raman spectra were recorded from five locations on each sample. Deconvolution of the 2D, G, D, and D' bands was conducted using XPSPeak 4.1 software, fitting them with Lorentzian line shapes. The 2D peak and G peak intensity ratio (I(2D)/I(G)) was employed to appraise the number of layers [50]. A reduction in this ratio implies an increase in the number of graphene layers. The ratio of the D peak intensity to the G peak intensity (I(D)/I(G)) was utilized to estimate the defect density within the graphene structure [51,52]. An increased ratio reflects a higher density of defects.

# 3. Results

## 3.1. I-V Characteristics

Typical current-voltage characteristics of investigated junctions with different h-BN layer thicknesses at room temperature are shown in Figure 2 (these current-voltage characteristics in semi-log scale are presented in Figure S2 in Supplement S2). No apparent differences are observed between the samples with a h-BN layer and without. At forward bias in the low-voltage regime and at reverse bias over a broader range, the current scales linearly with voltage, indicating dominant ohmic behavior. At higher forward voltages, a nonlinearity appears in all samples, indicating possible Schottky emission or other field-enhanced conduction mechanisms, such as Poole-Frenkel (PF) emission, direct tunneling, or Fowler-Nordheim tunneling. Such conduction mechanisms are often observed in graphene-based devices [11,17,53]. In graphene/semiconductor junctions, Schottky emission is widely accepted as a dominant conduction mechanism [3,11,16,17]. However, when an insulator, such as h-BN, is inserted between graphene and a semiconductor, the determination of current conduction requires special attention. For example, when direct tunneling is dominant, the Richardson coefficient in the Schottky equation should be modified with a transmission factor. This factor depends on the insulator thickness and the barrier height at the semiconductor/insulator interface [1,11].



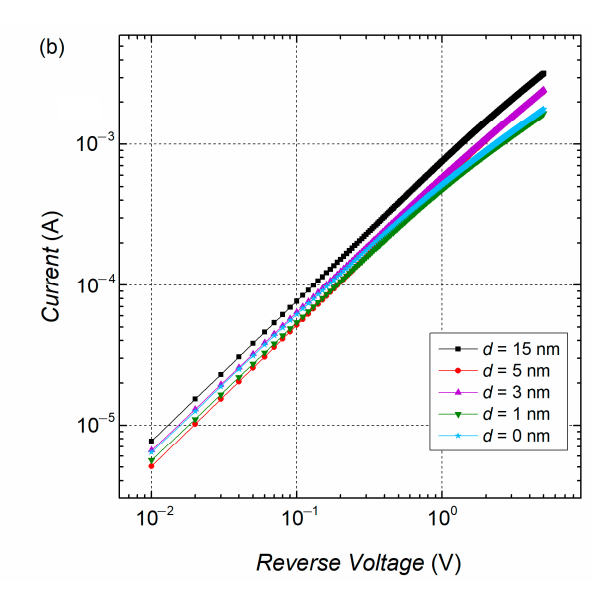


**Figure 2.** Typical current–voltage characteristics of the studied junctions at forward (**a**) and reverse (**b**) bias; *d*—h-BN interlayer thickness.

Crystals **2025**, 15, 747 6 of 16

Additionally, in such graphene/insulator/semiconductor structures, multiple conduction mechanisms can be active simultaneously or the dominant conduction mechanism can change with temperature. It should be noted that inhomogeneities at the interface, defects, conduction at grain boundaries, and barrier height fluctuations complicate the accurate identification of dominant conduction mechanisms [12,17,54]. The complexity in determining the Schottky vs. Poole–Frenkel emission from I-V characteristics measurement in our investigated samples is described in Supplement S3. That is where noise analysis helps. Ln(I) vs.  $\sqrt{U}$  and ln(I/U) vs.  $\sqrt{U}$  plots, which are usually employed for Schottky and Poole–Frenkel emission identification, are also presented in Figures S3 and S4. In the following section, the dominant conduction mechanism will be estimated based on the noise characteristics.

# 3.2. Low-Frequency Noise Spectra

All investigated samples exhibit 1/f or  $1/f^{\alpha}$ -type electrical fluctuations at forward and reverse bias. These fluctuations can be described as a superposition of many Lorentziantype noise spectral components resulting from individual fluctuators with widely distributed relaxation times. The representative noise spectra of the samples at forward and reverse bias are shown in Figure 3. Some junctions containing h-BN interlayers, investigated in this study, are distinguished by the Lorentzian-type noise spectra superimposed with 1/f components at low frequencies at forward bias at a specific range of flowing current. Several examples of electrical noise spectra with Lorentzian fluctuations are presented in Figure 4. In samples with a 5 nm thickness h-BN interlayer, Lorentzian-type noise spectra have been observed most frequently: in the current span from 0.05 mA to 0.1 mA and at higher currents from 0.75 mA to 3 mA. Additionally, a weak Lorentzian-type noise component has been observed in a junction with a 1 nm h-BN layer at 0.2 mA forward current (I<sub>F</sub>) (Figure 4). To facilitate clearer recognition of Lorentzian-type fluctuations, these spectra are commonly scaled by multiplying with frequency ( $S_{Uf}$ ) (Supplement S4, Figure S5). The Lorentzian-type noise spectrum is indicative of an isolated defect-related recombination site with a distinct relaxation time  $1/\tau_r = 1/\tau_e + 1/\tau_c$ , where  $\tau_e$  is the average time of electron emission, and  $\tau_c$  is the average electron capture time at the trap level [24]. In general, the current flow through the junction results in voltage noise due to variations in local resistance [25,55,56]. If the number of defects (both bulk and interface types) in the device is sufficiently high and the relaxation times are widely distributed, the 1/f noise spectrum is observed. The equation for 1/f noise intensity evaluation (Equation S4) and its description are provided in Supplement S4.

A "white" spectral region attributed to thermal noise is observed at low forward and reverse bias when f>2 kHz, as can be seen in Figure 3 at 0.005 mA and 0.01 mA currents. At such low currents, thermal noise is dominant and sets a limit for the minimum observable noise level. The intensity of thermal noise ( $S_U=4kTR_{\rm d}$ , k—Boltzmann's constant, T—temperature) is determined by the differential resistance  $R_{\rm d}$  of the investigated junction at the linear I-V characteristic part (for a representative sample of a 3 nm thickness h-BN layer in Figure 3,  $R_{\rm d}=1410~\Omega$ ). In some cases, thermal noise is masked by higher 1/f noise intensity. An example is illustrated in Figure 3b for a junction with a 5 nm h-BN layer at 0.01 mA.

Crystals **2025**, 15, 747 7 of 16

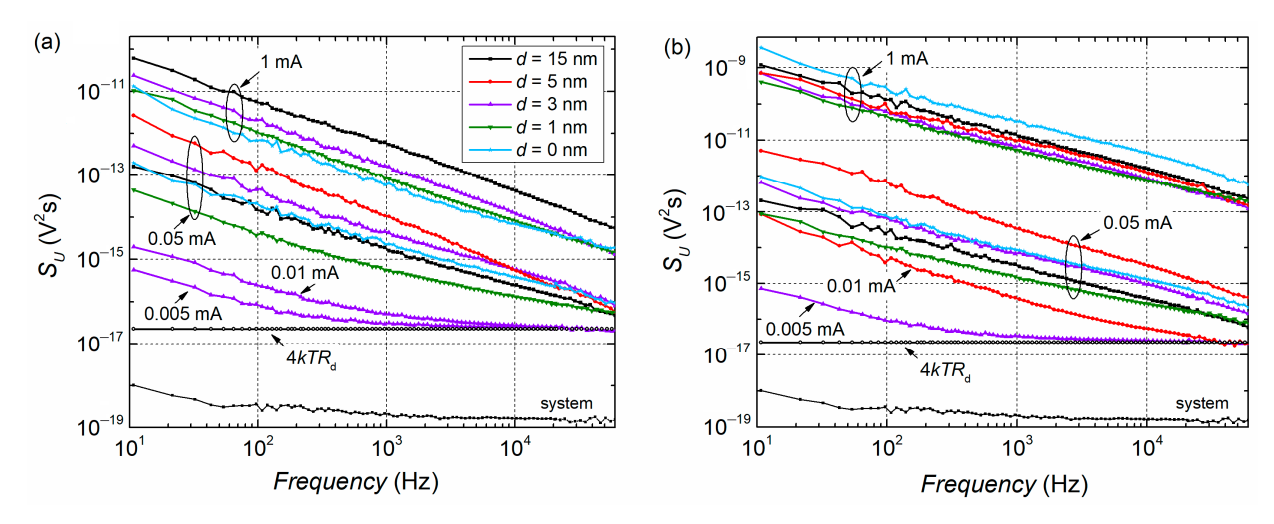


**Figure 3.** Representative spectra of low-frequency noise at different values of the forward (a) and reverse (b) current. The curve named "system" denotes the noise level of the measurement system; d—h-BN interlayer thickness. The legend is the same for (a,b) figures.

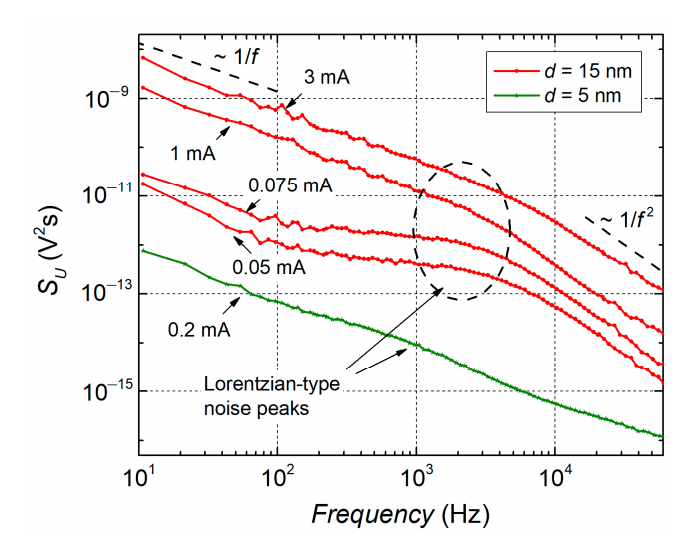


**Figure 4.** Electrical noise spectra with Lorentzian-type components at different forward current values; *d*—h-BN interlayer thickness.

# 3.3. Noise Spectral Density vs. Current Characteristics

The interdependence of the current noise spectral density  $S_I$  and the current I provides insight into the physical processes occurring at the junction and possible conduction mechanisms [3,23,35,57]. For this reason, the current noise spectral density has been calculated as  $S_I = S_U/R_d^2$ , where  $R_d$  denotes the differential resistance of the sample  $R_d = (dU/dI)$ . The current dependences of the differential resistance for representative samples shown in Figure 2 are depicted in Figure S6 (Supplement S5).

# 3.3.1. Influence of Grain Boundaries on Low-Frequency Noise

Figure 5 presents the different trends observed in the current spectral density for forward and reverse current in the samples investigated. In the current range, in which the *I-V* characteristic is linear, electrical noise  $S_I$  is proportional to  $I^\gamma$ , where  $\gamma$  is very close to 2 for all the investigated junctions. This is expected for ohmic samples, as Equation (S4) defines. At elevated forward bias, a discrepancy from the quadratic relationship in noise vs. current characteristic is observed, where  $S_I \sim I^\gamma$ , and  $\gamma > 2$ . The current intervals with a rapid increase in noise intensity coincide with the non-linear regions of the *I-V* characteristics. Such strong noise dependence on current with  $\gamma > 2$  is often attributed

Crystals **2025**, 15, 747 8 of 16

to the influence of grain boundaries (GB) and was earlier observed in polycrystalline films [23]. As a result of the nanocrystalline structure of graphene [39,48,58,59] and h-BN layers [45], grain boundaries are dominant defect sources in these devices. Accordingly, in the investigated graphene/h-BN/Si junctions, the observed  $S_I \sim I^3$  behavior confirms the dominant role of GBs as strong noise generators [30]. In graphene grown by CVD, GB prevailing results in a substantial increase in noise intensity compared to exfoliated graphene [36].

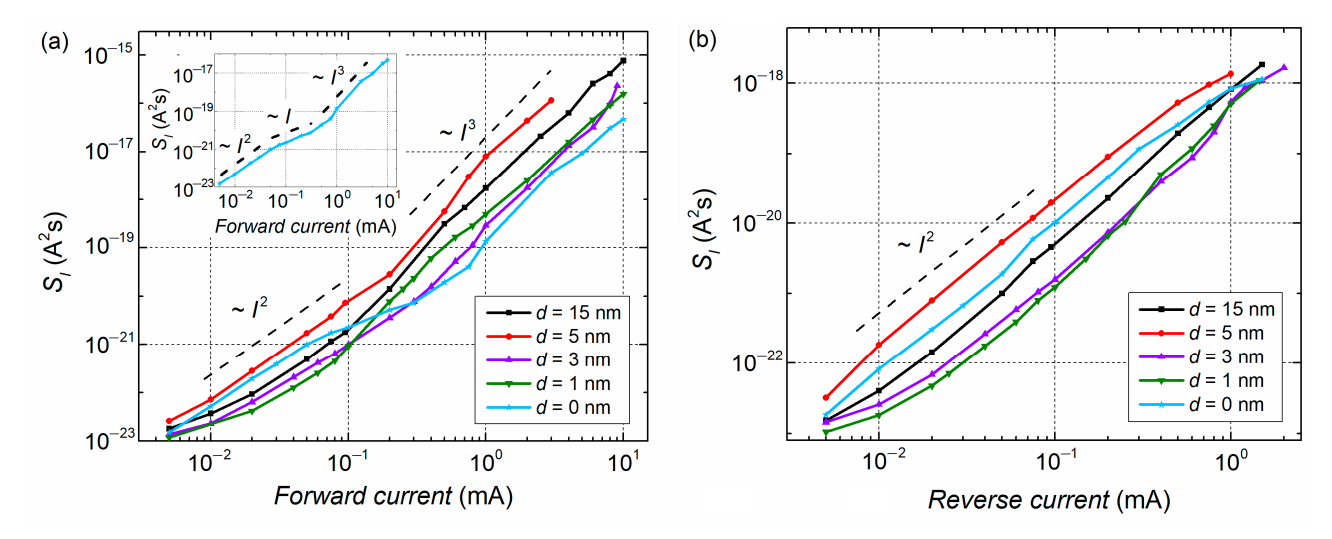


**Figure 5.** Typical graphs of current noise spectral density vs. forward (**a**) and reverse (**b**) current at 1044 Hz frequency; d—h-BN interlayer thickness. The inset in (**a**) represents the  $S_I(I)$  dependence of the reference sample.

However, reference samples without an h-BN layer are distinguished by different electrical noise vs. forward current characteristics (Figure 5a). An interval, in which  $S_I$  scales approximately linearly with current (i.e.,  $\gamma \approx 1$ ) is detected within the current range of 0.05 to 0.4 mA. At high currents, the influence of GBs plays a significant role in the rapid increase in noise intensity. The proportionality  $S_I \sim I$  am usually attributed to pure thermionic emission in Schottky diodes [3,57]. Such a dependence was not observed in samples with an h-BN layer, meaning that a different prevailing conduction mechanism or several conduction mechanisms are contributing simultaneously.

# 3.3.2. Identification of Poole-Frenkel Emission

Following the approach outlined in [60–62] for dominant Poole–Frenkel emission, the product of normalized current noise spectral density  $S_I/I^2$  and electrical field (which is proportional to the applied voltage U) should be constant regardless of the current and is proportional to the trap density and field enhancement factor of PF emission. A plateau in corresponding noise plots is observed at high reverse bias for samples with 15 nm and 5 nm thicknesses of the h-BN layer, suggesting the dominance of Poole–Frenkel emission. A trend has been observed—samples with thicker h-BN layers exhibit higher Poole–Frenkel conductivity at room temperature, as shown in Figure 6. The PF noise analysis at high forward bias was complicated by the influence of grain boundaries on noise characteristics. Only one sample with a 15 nm thickness h-BN layer demonstrated a narrow plateau in  $U \times S_I/I^2$  vs. current plot at high forward bias (Figure 6a), while no such region was observed in the 5 nm thickness h-BN samples. The PF charge transport mechanism has been reported for a small forward voltage range of the I-V characteristics of graphene/Al $_2$ O $_3$ /Si solar cells [11], a high reverse voltage range of the I-V characteristics of graphene/n-Si junctions [21], and reverse current flow via graphene/SiC junctions [9].

Crystals **2025**, 15, 747 9 of 16

The Poole–Frenkel emission from defects in h-BN was found in graphene/h-BN field effect transistors [10]. Similarly, in the present study, it is plausible that PF conduction arises from defects in the HIPIMS-deposited h-BN interlayer. Exfoliated h-BN layers or h-BN films grown by chemical vapor deposition on catalytic copper foil usually contain few defects, and their use can ensure the fabrication of graphene-based FETs with ultra-low noise. However, these technologies are not suited for industrial-scale semiconductor device fabrication. In our case, the boron nitride was grown directly on a silicon substrate using the HIPIMS technique, which is already used for large-scale manufacturing. In this case, higher defect density in the h-BN films can be supposed like [63].

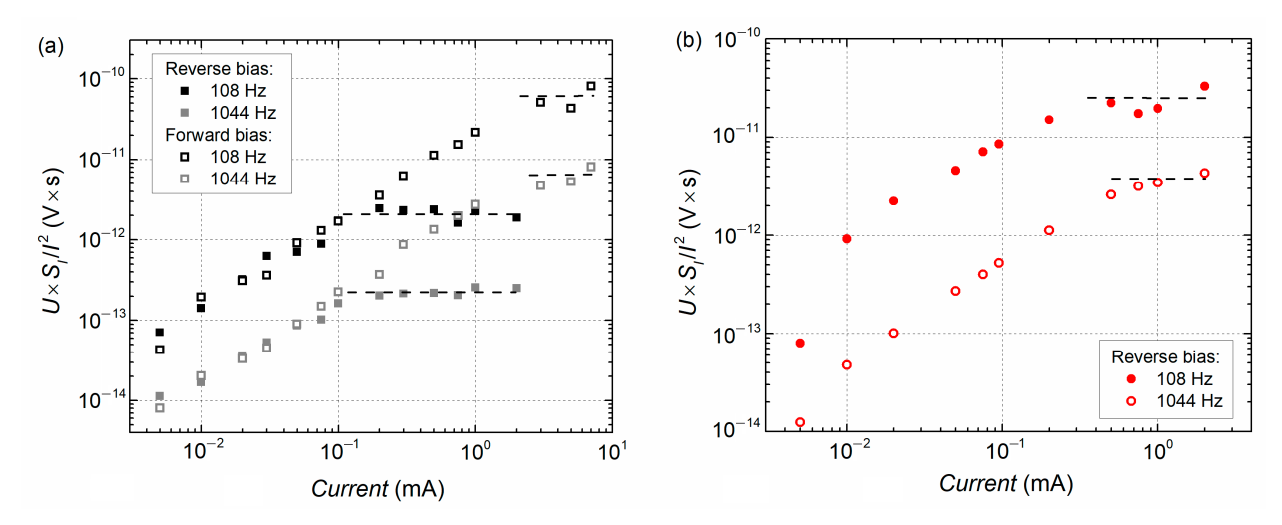


**Figure 6.**  $U \times S_I/I^2$  vs. current plots for 15 nm (**a**) and 5 nm (**b**) h-BN layer thickness samples at 108 Hz and 1044 Hz frequencies.

From the low-frequency noise perspective, the pronounced dominance of trap-assisted tunneling is usually linked to the appearance of shot noise in electrical noise spectra, modulated by the Fano factor [61]. However, no shot noise was observed in this experiment.

Here, in Figures 3–5, only representative noise curves or dependences of samples are represented. Direct comparison of noise intensity between different samples should rely on Figure 7a in the following Section 3.4, which summarizes the averaged data.

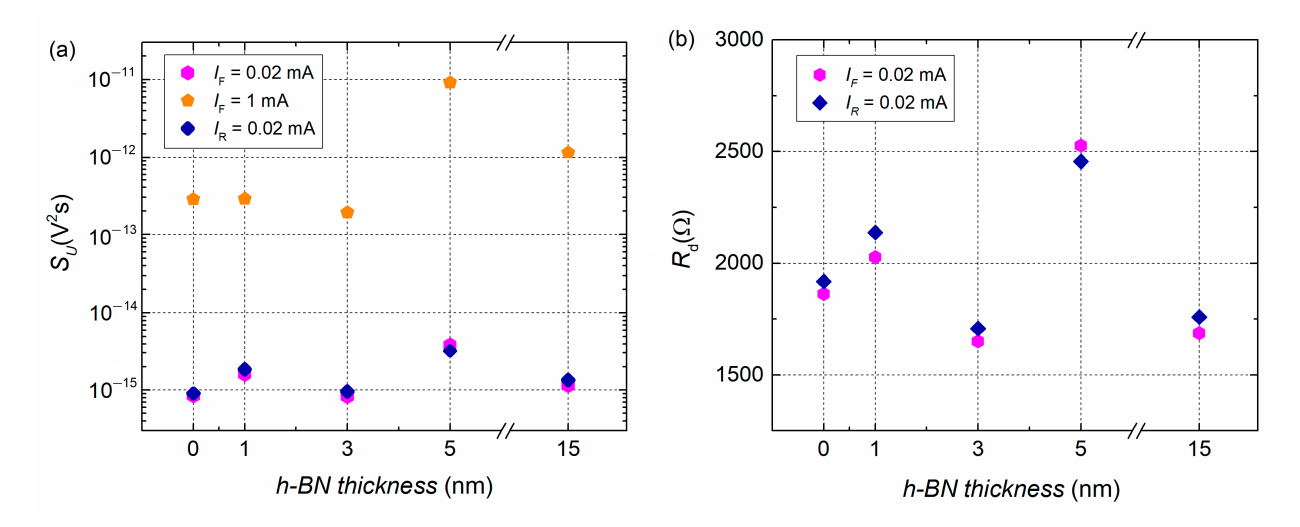


**Figure 7.** Average voltage noise spectral density values at a 1044 Hz frequency, reverse current of 0.02 mA, and forward current of 0.02 and 1 mA (a); differential resistance in the ohmic part of the current–voltage curve under positive and negative biasing conditions (b) of multiple graphene/h-BN/Si junction samples as a function of h-BN layer thickness.

3.4. Statistical Investigation and Defect Identification in Samples with Different H-BN Layer Thickness

# 3.4.1. Noise Intensity Between Samples with Different H-BN Layer Thickness

To compare the noise intensity between different samples and evaluate the impact of h-BN interlayer thickness on the graphene/h-BN/Si junctions through the low-frequency noise characterization, voltage noise spectral density values at 1044 Hz were extracted for multiple investigated samples within each h-BN thickness category. The average values of voltage noise spectral densities of the tested junctions are presented in Figure 7a. The comparison was made at different forward current levels (0.02 mA and 1 mA), corresponding to the linear and non-linear regions of the I-V characteristics (Figure 2), as well as at 0.02 mA of reverse bias. The noise intensity is not directly proportional to the h-BN thickness (Figure 7a). As a general trend, junctions with a 5 nm-thick h-BN interlayer demonstrated the highest noise intensity under all experimental conditions. The average voltage noise spectral density is very similar between specimens with h-BN interlayers under both forward and reverse biases in the linear *I-V* characteristic range, except for graphene/5 nm h-BN/Si samples (Figure 7a). However, under forward bias conditions, where the *I-V* behavior deviates from linearity, the fluctuation intensity of the thickest h-BN layer samples (5 nm and 15 nm) increases more compared to the increase in noise level of the 1 nm and 3 nm h-BN thickness samples ( $I_F = 1$  mA in Figure 7a).

This observation is consistent with the findings in Section 3.3, where a deviation from the  $S_I \sim I^2$  dependence and an enhanced  $\gamma > 2$  exponent were linked to grain boundaries (GBs) acting as dominant noise sources in nanocrystalline graphene and h-BN layers. These GB-related effects can also contribute to local current crowding and a further increase in 1/f noise [23,31]. Thus, it is important to consider in which mode (linear or non-linear I-V characteristic part) the device operates. As Figure 7b illustrates, a good correlation between the noise intensity and the differential resistance values of the investigated junctions in the linear I-V characteristic range is confirmed.

The reference junctions without h-BN interlayers are characterized by close (or even slightly lower) noise intensities as the remaining samples (except the graphene/5 nm h-BN/Si junctions) (Figure 7a). The values of differential resistances are also similar to the remaining samples (Figure 7b).

# 3.4.2. Assessment of Raman Spectra and Low-Frequency Noise Characteristics

Raman scattering spectra were studied to reveal structural parameters of the graphene and relate them to the low-frequency noise results. G and 2D peaks characteristic of graphene are apparent in those spectra (Supplement 6, Figure S7). The defect-related D band was found because directly deposited graphene is nanocrystalline, and another defect-related peak, D' peak, is observed as a shoulder of the G band. Afterward, the Raman spectra parameters were analyzed to reveal possible relations between the low-frequency noise and graphene's structural parameters.

It was revealed in our previous study that substrate-induced graphene self-doping is crucial for graphene/Si junction properties and that the insertion of an h-BN interlayer can partially suppress this effect, thereby enhancing the photoelectric and photovoltaic properties of the junction [4]. Analysis of the Pos(2D) vs. Pos(G) plot can provide valuable information on stress and doping of the graphene [64]. The Pos(2D) downshift with Pos(G) upshift, typical of n-type doping, was revealed for graphene grown directly on silicon and on the h-BN interlayer [4]. However, in the present research, no dependence of low-frequency noise on Pos(G) or Pos(2D) has been observed (Supplement S6, Figure S8). This indicates that substrate-induced graphene self-doping should not be considered the primary factor determining the noise characteristics at graphene/h-BN/Si junctions. Notably, no

apparent relationship between the spectral density of electrical noise and graphene's layer number (Supplement S6, Figure S9) has also been observed.

Non-monotonic noise increase in defect density is observed in graphene (Figure 8a). Initially, the noise clearly increases with the I(D)/I(G) ratio. However, for samples featuring an inserted 1 nm-thick h-BN interlayer, a significant reduction in the noise level is observed. To identify possible reasons for this inconsistency, the effects of different graphene defect types were investigated. For this reason, intensity ratios of the D and D' peaks were calculated. Three groups of the samples can be distinguished. In the case of the graphene/h-BN/Si junctions containing 3 nm, 5 nm, and 15 nm thickness boron nitride interlayers, the I(D)/I(D') value was about 2.5. That is between the value typical for grain boundary defects (3.5) and the value typical for on-site defects (1.3), which are commonly linked to hydrogen species bonded to the graphene [65]. In the case of the reference graphene sample, GB defects also prevail. However, considering these I(D)/I(D') values, the presence of some on-site defects is observed. Finally, for graphene/h-BN/Si(100) samples with an inserted 1 nm thickness h-BN interlayer, the I(D)/I(D') value appears to nearly match the typical value for grain boundaries (~3.6). It should be noted that the presence of some hydrogen bonds was revealed in HIPIMS-deposited h-BN films grown using a 152 sccm nitrogen gas flow using Raman spectroscopy [4]. In HIPIMS, hydrogen can originate from residual water vapor or hydrocarbons in the chamber; these species are dissociated in plasma and become bonded to boron or nitrogen at the growing film's surface, as was demonstrated in our previous research [4]. In the present study, such hydrogen incorporated in the h-BN layer could subsequently be released during the graphene's direct synthesis step and become incorporated into the growing graphene. For the 1 nm h-BN film, the absence of detectable hydrogen-related features in the graphene suggests that either hydrogen was initially negligible, or it was fully desorbed during synthesis at 700 °C. For thicker h-BN interlayers, hydrogen atoms could diffuse from the boron nitride into the graphene layer during growth, becoming incorporated into its structure.

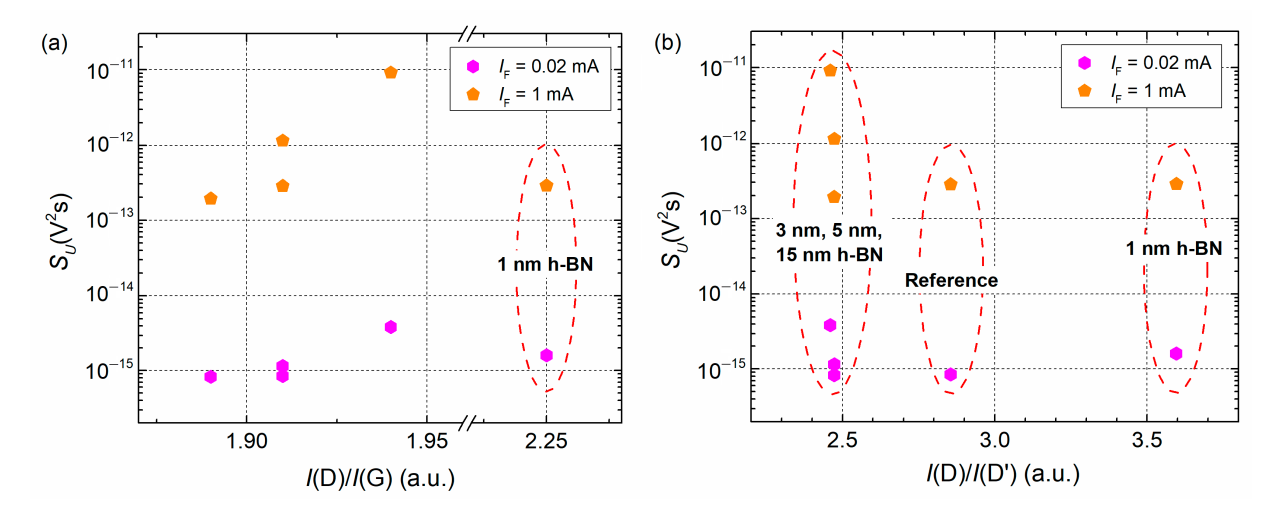


**Figure 8.** Average voltage noise spectral density vs. I(D)/I(G) (**a**) and I(D)/I(D') ratios (**b**). The  $S_U$  was measured using an  $I_F$  of 0.02 mA and 1 mA and a frequency of 1044 Hz.

It should be noted that in the case of graphene/Si junction X-ray detectors and graphene-based field-effect transistors, hydrogen-related defects can lead to a significant increase in low-frequency noise [66,67]. Thus, the existence of hydrogen-related structural irregularities in the graphene may be an important factor affecting the noise increase in the device. This explains the outstanding samples with 5 nm thickness h-BN layer in Figure 7. On the other hand, in our case, average voltage noise spectral density in the

Crystals 2025, 15, 747 12 of 16

graphene/1 nm h-BN/silicon junctions is not exceptionally large despite much higher grain boundary density indicated by high I(D)/I(G) proportion (Figure 8a). This effect was previously reported during earlier 1/f noise studies on graphene/silicon contacts [35]. It was attributed to an increase in charge carriers at the graphene grain boundaries, which act as dopants with very low excitation energies [35].

In general, several tendencies have been observed when comparing the results obtained in Section 3.3 with the analysis of Raman spectra. For reference, 3 nm, 5 nm, and 15 nm thickness h-BN samples, it can be stated that hydrogen-related defects are mainly responsible for the fluctuations observed in the linear I-V characteristic part and have an influence on the differential resistance of the investigated junctions, as demonstrated by a 5 nm thickness h-BN sample. At higher forward currents, the uneven noise increases between junctions with different h-BN thicknesses, as well as the change in  $S_I$  dependence on current, indicates that the influence of other defects, primarily grain boundaries, increases in addition to hydrogen-related defects. Furthermore, the inserted h-BN layer affects the low-frequency fluctuations in the non-linear I-V region, especially in the case of a thick h-BN layer (Figure 7a), when the GBs start to dominate the conduction.

## 4. Conclusions

A comprehensive assessment of the low-frequency electrical noise characteristics of graphene/h-BN/Si heterojunctions has been performed under both forward and reverse bias and compared with the graphene/silicon reference structure without the h-BN interlayer.

All investigated junctions exhibit 1/f-type electrical fluctuations at both forward and reverse bias, with the appearance of some Lorentzian-type noise components at specific forward current intervals. Low-frequency noise analysis indicates Schottky emission in reference graphene/Si junctions at room temperature. In contrast, samples with thicker h-BN interlayers (15 nm and 5 nm) exhibit signatures of Poole–Frenkel emission, with its contribution diminishing as the h-BN layer thickness decreases.

The statistical investigation of multiple samples across each h-BN layer thickness category, combined with analysis of graphene Raman spectra, reveals the presence of hydrogen-related defects in graphene and at the graphene/h-BN interface. These defects are responsible for the observed low-frequency fluctuations at low bias in the linear region of the device's current–voltage characteristic. Among the investigated junctions, the graphene/1 nm h-BN/Si structure showed a significantly reduced density of these defects.

A rapid increase in noise intensity in the non-linear junction I-V characteristic range, where current spectral density  $S_I$  scales as  $I^Y$  and  $\gamma > 2$ , is associated with the grain boundaries being dominant defects and acting as major noise sources due to the nanocrystalline structure of the graphene and h-BN layers.

Overall, the results demonstrate that h-BN interlayer thickness and defect composition play a critical role in governing low-frequency noise behavior, which is essential for optimizing graphene-based devices for sensing and optoelectronic applications.

**Supplementary Materials:** The following supporting information can be downloaded at: https://www.mdpi.com/article/10.3390/cryst15090747/s1, Figure S1. The noise measurement setup: A—an ammeter, ADC—an analog-to-digital converter, B—batteries, F—a filter system, LNA—a low-noise amplifier, PC—a personal computer,  $R_{\text{load}}$ —a load resistance,  $R_{\text{ref}}$ —a reference resistor, Sample—a graphene/h-BN/Si or graphene/Si junction under test, V—a voltmeter; Figure S2. Typical current-voltage characteristics of the investigated junctions at forward and reverse bias in semi-log scale; d—h-BN interlayer thickness; Figure S3. Plots of  $\ln(I)$  vs.  $\sqrt{U}$  (usually used for Schottky emission identification) for junctions with h-BN layer thickness of 15 nm (a) and 5 nm (b), and for the reference sample without the h-BN layer (c) at forward bias at different temperatures. Red lines are the linear

fits at room temperature; Figure S4. Plots of  $\ln(I/U)$  vs.  $\sqrt{U}$  (usually used for Poole–Frenkel emission identification) for junctions with h-BN layer thickness of 15 nm (a) and 5 nm (b), and for the reference sample without the h-BN layer (c) at forward bias at different temperatures. Red lines are the linear fits at room temperature; Figure S5. Normalized electrical noise spectra ( $S_{Uf}$ ) with Lorentzian-type components at different forward current values; d—h-BN interlayer thickness. The dashed area indicates where 1/f fluctuations dominate. The frequency of the maximum of the normalized voltage fluctuation spectral density  $f_0$  denotes the relaxation time as  $\tau_{\rm r}=1/(2\pi f_0)$ ; Figure S6. Dependences of the differential resistance on forward (a) and reverse (b) currents for samples shown in Figure 2; d—h-BN interlayer thickness; Figure S7. Typical Raman scattering spectra of the graphene samples; Figure S8. Dependences of average voltage noise spectral density on Pos(2D) (a) and Pos(G) (b) at forward currents of 0.02 mA and 1 mA at 1044 Hz frequency; Figure S9. Dependence of average voltage noise spectral density on I(2D)/I(G) ratio at forward currents of 0.02 mA and 1 mA at 1044 Hz frequency; Table S1. Experimental slope values from linear fit in the high-bias regime at 295 K for graphene/h-BN/Si samples and the reference graphene/Si junction. References [9,25,55,56,68,69] are cited in the Supplementary Materials.

**Author Contributions:** Conceptualization, J.G., J.M. and Š.M.; methodology, J.M. and Š.M.; validation, J.G. and Š.J.; formal analysis, J.G. and I.P.; investigation, J.G., I.P., A.V., Š.J. and R.G.; resources, J.G., R.G. and A.V.; writing—original draft preparation, J.G., J.M. and Š.M.; writing—review and editing, J.G., J.M. and Š.M.; visualization, J.G., I.P. and Š.J.; supervision, J.M. and Š.M.; project administration, Š.M.; funding acquisition, Š.M. All authors have read and agreed to the published version of the manuscript.

**Funding:** This study was funded by the Research Council of Lithuania (Proposal No. P-MIP-22-235; Contract No. S-MIP-22-67).

Data Availability Statement: Data is contained within the article or supplementary material.

Conflicts of Interest: The authors declare no conflicts of interest.

# **Abbreviations**

The following abbreviations are used in this manuscript:

h-BN Hexagonal boron nitride

HIPIMS High power impulse magnetron sputtering
PECVD Plasma-enhanced chemical vapor deposition

CVD Chemical vapor deposition FET Field-effect transistor

 $S_U$  Spectral density of voltage fluctuations'  $S_I$  Spectral density of current fluctuations'  $S_R$  Spectral density of resistance fluctuations'

I-V characteristics Current-voltage characteristics

RdDifferential resistancePos(G)Position of G peakPos(2D)Position of 2D peakPF emissionPoole–Frenkel emissionGBGrain boundaries

# References

- 1. Wang, C.; Behura, S.K.; Berry, V. Temperature Dependent Device Characteristics of Graphene/H-BN/Si Heterojunction. *Semicond. Sci. Technol.* **2020**, *35*, 075020. [CrossRef]
- 2. Shen, J.; Liu, X.; Song, X.; Li, X.; Wang, J.; Zhou, Q.; Luo, S.; Feng, W.; Wei, X.; Lu, S.; et al. High-Performance Schottky Heterojunction Photodetector with Directly Grown Graphene Nanowalls as Electrodes. *Nanoscale* 2017, *9*, 6020–6025. [CrossRef]
- 3. An, Y.; Behnam, A.; Pop, E.; Bosman, G.; Ural, A. Forward-Bias Diode Parameters, Electronic Noise, and Photoresponse of Graphene/Silicon Schottky Junctions with an Interfacial Native Oxide Layer. *J. Appl. Phys.* **2015**, *118*, 114307. [CrossRef]

4. Meškinis, Š.; Jankauskas, Š.; Vasiliauskas, A.; Stankus, V.; Guobienė, A.; Lukoševičius, K.; Jasutis, A.; Gudaitis, R. Graphene Direct Growth by Microwave PECVD on H-BN Films Deposited by Reactive HIPIMS. *Nano Ex.* **2025**, *6*, 025007. [CrossRef]

- 5. An, Y.; Behnam, A.; Pop, E.; Ural, A. Metal-Semiconductor-Metal Photodetectors Based on Graphene/P-Type Silicon Schottky Junctions. *Appl. Phys. Lett.* **2013**, 102, 013110. [CrossRef]
- 6. Zhu, M.; Li, X.; Li, X.; Zang, X.; Zhen, Z.; Xie, D.; Fang, Y.; Zhu, H. Schottky Diode Characteristics and 1/f Noise of High Sensitivity Reduced Graphene Oxide/Si Heterojunction Photodetector. *J. Appl. Phys.* **2016**, *119*, 124303. [CrossRef]
- 7. Kalita, G.; Shaarin, M.D.; Paudel, B.; Mahyavanshi, R.; Tanemura, M. Temperature Dependent Diode and Photovoltaic Characteristics of Graphene-GaN Heterojunction. *Appl. Phys. Lett.* **2017**, *111*, 013504. [CrossRef]
- 8. Li, H.; Shi, Y.; Shang, H.; Wang, W.; Lu, J.; Zakharov, A.A.; Hultman, L.; Uhrberg, R.I.G.; Syväjärvi, M.; Yakimova, R.; et al. Atomic-Scale Tuning of Graphene/Cubic SiC Schottky Junction for Stable Low-Bias Photoelectrochemical Solar-To-Fuel Conversion. *ACS Nano* 2020, 14, 4905–4915. [CrossRef]
- 9. Tomer, D.; Rajput, S.; Hudy, L.J.; Li, C.H.; Li, L. Carrier Transport in Reverse-Biased Graphene/Semiconductor Schottky Junctions. *Appl. Phys. Lett.* **2015**, *106*, 173510. [CrossRef]
- 10. Quezada-Lopez, E.A.; Joucken, F.; Chen, H.; Lara, A.; Davenport, J.L.; Hellier, K.; Taniguchi, T.; Watanabe, K.; Carter, S.; Ramirez, A.P.; et al. Persistent and Reversible Electrostatic Control of Doping in Graphene/Hexagonal Boron Nitride Heterostructures. *J. Appl. Phys.* **2020**, 127, 044303. [CrossRef]
- 11. Wong, H.; Zhang, J.; Liu, J.; Anwar, M.A. On the Current Conduction and Interface Passivation of Graphene–Insulator–Silicon Solar Cells. *Nanomaterials* **2025**, *15*, 416. [CrossRef]
- 12. Tomer, D.; Rajput, S.; Hudy, L.J.; Li, C.H.; Li, L. Inhomogeneity in Barrier Height at Graphene/Si (GaAs) Schottky Junctions. *Nanotechnology* **2015**, *26*, 215702. [CrossRef]
- 13. Afzal, A.M.; Imran, M.; Iqbal, M.W.; Iqbal, M.Z.; Mumtaz, S.; Azeem, M.; Dastgeer, G.; Al-Ammar, E.A.; Ali, A. Surface Modification and Interface Engineering to Enhance the Performance of 2D-Graphene/3D-Silicon Schottky Junction Solar Cells. *J. Mater. Sci. Mater. Electron.* 2024, 35, 2165. [CrossRef]
- 14. Sinha, D.; Lee, J.U. Ideal Graphene/Silicon Schottky Junction Diodes. Nano Lett. 2014, 14, 4660–4664. [CrossRef] [PubMed]
- 15. Li, X.; Zhu, M.; Du, M.; Lv, Z.; Zhang, L.; Li, Y.; Yang, Y.; Yang, T.; Li, X.; Wang, K.; et al. High Detectivity Graphene-Silicon Heterojunction Photodetector. *Small* **2015**, *12*, 595–601. [CrossRef]
- 16. Doukas, S.; Mensz, P.; Myoung, N.; Ferrari, A.C.; Goykhman, I.; Lidorikis, E. Thermionic Graphene/Silicon Schottky Infrared Photodetectors. *Phys. Rev. B* **2022**, *105*, 115417. [CrossRef]
- 17. Pelella, A.; Grillo, A.; Faella, E.; Luongo, G.; Askari, M.B.; Di Bartolomeo, A. Graphene-Silicon Device for Visible and Infrared Photodetection. *ACS Appl. Mater. Interfaces* **2021**, *13*, 47895–47903. [CrossRef]
- 18. Ying, X.; Li, K.; Liu, L.; Wang, J.; Jiang, Y.; Xu, J.; Liu, Z. Spectral Photovoltaic Response of Graphene-Silicon Heterojunction. *Appl. Phys. Lett.* **2017**, *111*, 251106. [CrossRef]
- 19. Casalino, M.; Russo, R.; Russo, C.; Ciajolo, A.; Di Gennaro, E.; Iodice, M.; Coppola, G. Free-Space Schottky Graphene/Silicon Photodetectors Operating at 2 μm. *ACS Photonics* **2018**, *5*, 4577–4585. [CrossRef]
- Selvi, H.; Unsuree, N.; Whittaker, E.; Halsall, M.P.; Hill, E.W.; Thomas, A.; Parkinson, P.; Echtermeyer, T.J. Towards Substrate Engineering of Graphene–Silicon Schottky Diode Photodetectors. *Nanoscale* 2018, 10, 3399–3409. [CrossRef]
- 21. Wong, H.; Anwar, M.A.; Dong, S. Effects of Silicon Surface Defects on the Graphene/Silicon Schottky Characteristics. *Results Phys.* **2021**, *29*, 104744. [CrossRef]
- 22. Jones, B.K. Electrical Noise as a Reliability Indicator in Electronic Devices and Components. *IEE Proc. Circ. Dev. Syst.* **2002**, 149, 13–22. [CrossRef]
- 23. Vandamme, L.K.J. Noise as a Diagnostic Tool for Quality and Reliability of Electronic Devices. *IEEE Trans. Electron Dev.* **1994**, 41, 2176–2187. [CrossRef]
- 24. Kirton, M.J.; Uren, M.J. Noise in Solid-State Microstructures: A New Perspective on Individual Defects, Interface States and Low-Frequency (1/f) Noise. *Adv. Phys.* **1989**, *38*, 367–468. [CrossRef]
- 25. Palenskis, V.; Maknys, K. Nature of Low-Frequency Noise in Homogeneous Semiconductors. *Sci. Rep.* **2015**, *5*, 18305. [CrossRef] [PubMed]
- 26. Balandin, A.A. Low-Frequency 1/f Noise in Graphene Devices. Nat. Nanotechnol. 2013, 8, 549–555. [CrossRef]
- Arnold, H.N.; Sangwan, V.K.; Schmucker, S.W.; Cress, C.D.; Luck, K.A.; Friedman, A.L.; Robinson, J.T.; Marks, T.J.; Hersam, M.C. Reducing Flicker Noise in Chemical Vapor Deposition Graphene Field-Effect Transistors. *Appl. Phys. Lett.* 2016, 108, 073108.
   [CrossRef]
- 28. Kumar, A.; Kashid, R.; Ghosh, A.; Kumar, V.; Singh, R. Enhanced Thermionic Emission and Low 1/f Noise in Exfoliated Graphene/GaN Schottky Barrier Diode. *ACS Appl. Mater. Inter.* **2016**, *8*, 8213–8223. [CrossRef]
- 29. Karnatak, P.; Paul, T.; Islam, S.; Ghosh, A. 1/f Noise in van Der Waals Materials and Hybrids. *Adv. Phys. X* **2017**, 2, 428–449. [CrossRef]

30. Kochat, V.; Tiwary, C.S.; Biswas, T.; Ramalingam, G.; Hsieh, K.; Chattopadhyay, K.; Raghavan, S.; Jain, M.; Ghosh, A. Magnitude and Origin of Electrical Noise at Individual Grain Boundaries in Graphene. *Nano Lett.* **2015**, *16*, 562–567. [CrossRef]

- 31. Karnatak, P.; Sai, T.P.; Goswami, S.; Ghatak, S.; Kaushal, S.; Ghosh, A. Current Crowding Mediated Large Contact Noise in Graphene Field-Effect Transistors. *Nat. Commun.* **2016**, *7*, 13703. [CrossRef]
- 32. Behera, A.K.; Harris, C.T.; Pete, D.V.; Smyth, C.M.; Muniz, M.B.; Koybasi, O.; Taniguchi, T.; Watanabe, K.; Belle, B.D.; Das, S.R. Charge-Inhomogeneity-Mediated Low-Frequency Noise in One-Dimensional Edge-Contacted Graphene Heterostructure Field Effect Transistors. *ACS Appl. Nano Mater.* **2024**, *7*, 12366–12375. [CrossRef]
- 33. Kakkar, S.; Karnatak, P.; Aamir, A.; Watanabe, K.; Taniguchi, T.; Ghosh, A. Optimal Architecture for Ultralow Noise Graphene Transistors at Room Temperature. *Nanoscale* **2020**, *12*, 17762–17768. [CrossRef]
- 34. Liu, G.; Stillman, W.; Rumyantsev, S.; Shao, Q.; Shur, M.; Balandin, A.A. Low-Frequency Electronic Noise in the Double-Gate Single-Layer Graphene Transistors. *Appl. Phys. Lett.* **2009**, *95*, 033103. [CrossRef]
- 35. Glemža, J.; Palenskis, V.; Gudaitis, R.; Jankauskas, Š.; Guobienė, A.; Vasiliauskas, A.; Meškinis, Š.; Pralgauskaitė, S.; Matukas, J. Low-Frequency Noise of Directly Synthesized Graphene/Si(100) Junction. *Diam. Relat. Mater.* **2022**, 127, 109207. [CrossRef]
- 36. Kochat, V.; Sahoo, A.; Pal, A.N.; Eashwer, S.; Ramalingam, G.; Sampathkumar, A.; Tero, R.; Thu, T.V.; Kaushal, S.; Okada, H.; et al. Origin of 1/f Noise in Graphene Produced for Large-Scale Applications in Electronics. *IET Circ. Device Syst.* **2015**, *9*, 52–58. [CrossRef]
- 37. Haigh, S.J.; Gholinia, A.; Jalil, R.; Romani, S.; Britnell, L.; Elias, D.C.; Novoselov, K.S.; Ponomarenko, L.A.; Geim, A.K.; Gorbachev, R. Cross-Sectional Imaging of Individual Layers and Buried Interfaces of Graphene-Based Heterostructures and Superlattices. *Nat. Mater.* **2012**, *11*, 764–767. [CrossRef]
- 38. Chugh, S.; Mehta, R.; Lu, N.; Dios, F.D.; Kim, M.J.; Chen, Z. Comparison of Graphene Growth on Arbitrary Non-Catalytic Substrates Using Low-Temperature PECVD. *Carbon* **2015**, *93*, 393–399. [CrossRef]
- 39. Khan, A.; Islam, S.M.; Ahmed, S.; Kumar, R.R.; Habib, M.R.; Huang, K.; Hu, M.; Yu, X.; Yang, D. Direct CVD Growth of Graphene on Technologically Important Dielectric and Semiconducting Substrates. *Adv. Sci.* **2018**, *5*, 1800050. [CrossRef]
- 40. Meškinis, Š.; Gudaitis, R.; Vasiliauskas, A.; Guobienė, A.; Jankauskas, Š.; Stankevič, V.; Keršulis, S.; Stirkė, A.; Andriukonis, E.; Melo, W.; et al. Biosensor Based on Graphene Directly Grown by MW-PECVD for Detection of COVID-19 Spike (S) Protein and Its Entry Receptor ACE2. *Nanomaterials* **2023**, *13*, 2373. [CrossRef]
- 41. Han, Z.; Li, M.; Li, L.; Jiao, F.; Wei, Z.; Geng, D.; Hu, W. When Graphene Meets White Graphene—Recent Advances in the Construction of Graphene and *h*-BN Heterostructures. *Nanoscale* **2021**, *13*, 13174–13194. [CrossRef]
- 42. Wang, M.; Jang, S.K.; Jang, W.-J.; Kim, M.; Park, S.-Y.; Kim, S.-W.; Kahng, S.-J.; Choi, J.-Y.; Ruoff, R.S.; Song, Y.J.; et al. A Platform for Large-Scale Graphene Electronics—CVD Growth of Single-Layer Graphene on CVD-Grown Hexagonal Boron Nitride. *Adv. Mater.* 2013, 25, 2746–2752. [CrossRef]
- 43. Yang, W.; Chen, G.; Shi, Z.; Liu, C.-C.; Zhang, L.; Xie, G.; Cheng, M.; Wang, D.; Yang, R.; Shi, D.; et al. Epitaxial Growth of Single-Domain Graphene on Hexagonal Boron Nitride. *Nat. Mater.* **2013**, *12*, 792–797. [CrossRef]
- 44. Song, X.; Sun, J.; Qi, Y.; Gao, T.; Zhang, Y.; Liu, Z. Graphene/h-BN Heterostructures: Recent Advances in Controllable Preparation and Functional Applications. *Adv. Energy Mater.* **2016**, *6*, 1600541. [CrossRef]
- 45. Entani, S.; Takizawa, M.; Li, S.; Naramoto, H.; Sakai, S. Growth of Graphene on SiO<sub>2</sub> with Hexagonal Boron Nitride Buffer Layer. *Appl. Surf. Sci.* **2019**, *475*, 6–11. [CrossRef]
- 46. Won, U.Y.; Lee, B.H.; Kim, Y.R.; Kang, W.T.; Lee, I.; Kim, J.E.; Lee, Y.H.; Yu, W.J. Efficient Photovoltaic Effect in Graphene/h-BN/Silicon Heterostructure Self-Powered Photodetector. *Nano Res.* **2021**, *14*, 1967–1972. [CrossRef]
- 47. Stankus, V.; Vasiliauskas, A.; Guobienė, A.; Andrulevičius, M.; Meškinis, Š. Synthesis and Characterization of Boron Nitride Thin Films Deposited by High-Power Impulse Reactive Magnetron Sputtering. *Molecules* **2024**, *29*, 5247. [CrossRef] [PubMed]
- 48. Meškinis, Š.; Vasiliauskas, A.; Guobienė, A.; Talaikis, M.; Niaura, G.; Gudaitis, R. The Direct Growth of Planar and Vertical Graphene on Si(100) Via Microwave Plasma Chemical Vapor Deposition: Synthesis Conditions Effects. *RSC Adv.* 2022, 12, 18759–18772. [CrossRef] [PubMed]
- 49. Jankauskas, Š.; Gudaitis, R.; Vasiliauskas, A.; Guobienė, A.; Meškinis, Š. The Graphene Structure's Effects on the Current-Voltage and Photovoltaic Characteristics of Directly Synthesized Graphene/N-Si(100) Diodes. *Nanomaterials* **2022**, *12*, 1640. [CrossRef] [PubMed]
- 50. Hwang, J.-S.; Lin, Y.-H.; Hwang, J.-Y.; Chang, R.; Chattopadhyay, S.; Chen, C.-J.; Chen, P.; Chiang, H.-P.; Tsai, T.-R.; Chen, L.-C.; et al. Imaging Layer Number and Stacking Order through Formulating Raman Fingerprints Obtained from Hexagonal Single Crystals of Few Layer Graphene. *Nanotechnology* **2012**, 24, 015702. [CrossRef]
- 51. Childres, I.; Jauregui, L.A.; Tian, J.; Chen, Y.P. Effect of Oxygen Plasma Etching on Graphene Studied Using Raman Spectroscopy and Electronic Transport Measurements. *New J. Phys.* **2011**, *13*, 025008. [CrossRef]
- 52. Dresselhaus, M.S.; Ado, J.; Souza, G.; Saito, R. Defect Characterization in Graphene and Carbon Nanotubes Using Raman Spectroscopy. *Philos. Trans. R. Soc. A* **2010**, *368*, 5355–5377. [CrossRef]

53. Gupta, S.; Joshi, P.; Sachan, R.; Narayan, J. Fabricating Graphene Oxide/h-BN Metal Insulator Semiconductor Diodes by Nanosecond Laser Irradiation. *Nanomaterials* **2022**, *12*, 2718. [CrossRef]

- 54. Parui, S.; Ruiter, R.; Zomer, P.J.; Wojtaszek, M.; van Wees, B.J.; Banerjee, T. Temperature Dependent Transport Characteristics of Graphene/N-Si Diodes. *J. Appl. Phys.* **2014**, *116*, 244505. [CrossRef]
- 55. Palenskis, V. The Charge Carrier Capture–Emission Process—The Main Source of the Low-Frequency Noise in Homogeneous Semiconductors. *Lith. J. Phys.* **2017**, *56*, 200–206. [CrossRef]
- 56. Palenskis, V.; Pralgauskaitė, S.; Matukas, J.; Glemža, J. Description of the Low-Frequency Noise for Homogeneous Semiconductors. In Proceedings of the 2023 International Conference on Noise and Fluctuations (ICNF), Grenoble, France, 17–20 October 2023. [CrossRef]
- 57. Luo, M.-Y.; Bosman, G.; Der, V.; Hench, L.L. Theory and Experiments of 1/*f* Noise in Schottky-Barrier Diodes Operating in the Thermionic-Emission Mode. *IEEE Trans. Electron Dev.* **1988**, *35*, 1351–1356. [CrossRef]
- 58. Meškinis, Š.; Gudaitis, R.; Vasiliauskas, A.; Tamulevičius, S.; Niaura, G. Multiwavelength Raman Scattering Spectroscopy Study of Graphene Synthesized on Si(100) and SiO<sub>2</sub> by Microwave Plasma-Enhanced Chemical Vapor Deposition. *Phys. Status Solidi Rapid Res. Lett.* **2019**, *14*, 1900462. [CrossRef]
- 59. Rajackaitė, E.; Peckus, D.; Gudaitis, R.; Andrulevičius, M.; Tamulevičius, T.; Volyniuk, D.; Meškinis, Š.; Tamulevičius, S. Transient Absorption Spectroscopy as a Promising Optical Tool for the Quality Evaluation of Graphene Layers Deposited by Microwave Plasma. Surf. Coat. Technol. 2020, 395, 125887. [CrossRef]
- 60. Angelis, C.T.; Dimitriadis, C.A.; Samaras, I.; Brini, J.; Kamarinos, G.; Gueorguiev, V.K.; Ivanov, T.E. Study of Leakage Current in N-Channel and P-Channel Polycrystalline Silicon Thin-Film Transistors by Conduction and Low Frequency Noise Measurements. *J. Appl. Phys.* **1997**, *82*, 4095–4101. [CrossRef]
- 61. Shin, W.; Min, K.K.; Bae, J.-H.; Yim, J.; Kwon, D.; Kim, Y.; Yu, J.; Hwang, J.; Park, B.-G.; Kwon, D.; et al. Comprehensive and Accurate Analysis of the Working Principle in Ferroelectric Tunnel Junctions Using Low-Frequency Noise Spectroscopy. *Nanoscale* 2022, 14, 2177–2185. [CrossRef]
- 62. Im, K.-S.; Shin, S.; Jang, C.-H.; Cha, H.-Y. Low-Frequency Noise Characteristics in HfO<sub>2</sub>-Based Metal-Ferroelectric-Metal Capacitors. *Materials* **2022**, *15*, 7475. [CrossRef] [PubMed]
- 63. Singhal, R.; Echeverria, E.; McIlroy, D.N.; Singh, R.N. Synthesis of Hexagonal Boron Nitride Films on Silicon and Sapphire Substrates by Low-Pressure Chemical Vapor Deposition. *Thin Solid Film.* **2021**, 733, 138812. [CrossRef]
- 64. Lee, J.E.; Ahn, G.; Shim, J.; Lee, Y.S.; Ryu, S. Optical Separation of Mechanical Strain from Charge Doping in Graphene. *Nat. Commun.* **2012**, *3*, 1024. [CrossRef] [PubMed]
- 65. Eckmann, A.; Felten, A.; Mishchenko, A.; Britnell, L.; Krupke, R.; Novoselov, K.S.; Casiraghi, C. Probing the Nature of Defects in Graphene by Raman Spectroscopy. *Nano Lett.* **2012**, *12*, 3925–3930. [CrossRef]
- 66. Deng, N.; Wang, P.; Zhang, E.; Guo, B.; Li, D.; Ma, B.; Fleetwood, D.M.; Tian, H.; Zhang, J. Low-Frequency 1/f Noise in a Graphene/Silicon X-Ray Detector. In Proceedings of the IEEE International Conference on Manipulation, Manufacturing and Measurement on the Nanoscale (3M-NANO), Xi'an, China, 2–6 August 2021; pp. 1–4. [CrossRef]
- 67. Wang, P.; Perini, C.; O'Hara, A.; Tuttle, B.R.; Zhang, E.X.; Gong, H.; Liang, C.; Jiang, R.; Liao, W.; Fleetwood, D.M.; et al. Radiation-Induced Charge Trapping and Low-Frequency Noise of Graphene Transistors. *IEEE Trans. Nucl. Sci.* 2018, 65, 156–163. [CrossRef]
- 68. Sze, S.M.; Ng, K.K. Physics of Semiconductor Devices, 3rd ed.; John Wiley & Sons, Inc.: Hoboken, NJ, USA, 2007; pp. 227–228.
- 69. Kajen, R.S.; Chandrasekhar, N.; Pey, K.L.; Vijila, C.; Jaiswal, M.; Saravanan, S.; Ng, A.M.H.; Wong, C.P.; Loh, K.P. Charge Transport in Lightly Reduced Graphene Oxide: A Transport Energy Perspective. *J. Appl. Phys.* **2013**, *113*, 0637110. [CrossRef]

**Disclaimer/Publisher's Note:** The statements, opinions and data contained in all publications are solely those of the individual author(s) and contributor(s) and not of MDPI and/or the editor(s). MDPI and/or the editor(s) disclaim responsibility for any injury to people or property resulting from any ideas, methods, instructions or products referred to in the content.